Acta Materialia 155 (2018) 43–55

Contents lists available at ScienceDirect

Acta Materialia

journal homepage: www.elsevier.com/locate/actamat

Full length article

A unified theory for microstructural alterations in bearing steels under rolling contact fatigue

Hanwei Fu, Pedro E.J. Rivera-Díaz-del-Castillo*

Department of Engineering, Engineering Building, Lancaster University, LA1 4YW, UK

ARTICLE INFO

Article history:
Received 28 February 2018
Received in revised form
21 May 2018
Accepted 23 May 2018
Available online 26 May 2018

Keywords:
Rolling contact fatigue
Bearing steels
White etching areas
Dark etching regions
White etching bands

ABSTRACT

Three major types of microstructural alterations occurring under rolling contact fatigue, white etching areas (WEAs), dark etching regions (DERs) and white etching bands (WEBs), are modelled under a unified approach: dislocation-assisted carbon migration theory. Following our previous work on DERs and WEBs, a novel model is proposed to describe dislocation cell formation in WEAs. The proposed model yields predictions of WEAs appearance, agreeing with experimental observations. Bearing life can be estimated by the WEA appearance model. The three microstructural alterations models are combined and, for the first time, it becomes possible to predict the occurrence and the formation progress of WEAs, DERs and WEBs with a unified theory. Microstructural alteration maps are plotted as a function of number of cycles, temperature, contact pressure and stress cycle frequency. The models are validated by the experimental results reported over the last 50 years.

1. Introduction

Bearings are amongst the most vital steel components in modern machinery, finding their application in a wide range of fields such as vehicles, wind turbines and aerospace. The service conditions, however, can be damaging for the material; such damage can be accelerated by increasing contact pressure and temperature [1,2]. Under such circumstances, rolling components, in spite of being manufactured with high strength martensitic steels, are prone to failure due to rolling contact fatigue (RCF). Surface-induced spalling and pitting can be effectively eliminated with proper lubrication [3] whilst subsurface-induced RCF is almost unavoidable because of the unique Hertzian subsurface stress states, where the shear stress components peak at the subsurface [4]. Such shearing can induce microstructural alterations of three major types: white etching areas (WEAs), dark etching regions (DERs) and white etching bands (WEBs) [5]; occurring at different stages in bearing life, they alter the mechanical properties of the material and make the component prone to failure [6]. These microstructural alterations can be observed from the circumferential or axial section of a RCF tested bearing inner ring, as shown in Fig. 1. After surface preparation (grinding and polishing), they can be revealed by etching with 2% nital. For a given bearing steel, the formation of the microstructural alterations is controlled by RCF testing conditions such as contact pressure (p_0), temperature (T), stress cycle frequency ($\dot{N}$) and number of stress cycles (N).

WEAs appear at the early stage of bearing life, around $0.001L_{10}$ [7], where L_{10} is the number of stress cycles for 10% sample failure. They are frequently found adjacent to cracks initiated from non-metallic inclusions such as Al_2O_3 [8], although studies [9–11] showed that primary carbides can also produce WEAs. Fig. 2 (a) shows a pair of WEAs in the circumferential section of a fatigued rod, decorating the cracks generated on both sides of an inclusion. Due to their wing-type shape, WEAs are also referred to as butterflies [12]. As shown in Fig. 2 (a), WEAs exhibit unique directionality, typically 45° to the over-rolling direction (ORD), which should stem from the maximum shear stress at the subsurface [8]. The formation of WEAs is a process of martensite decay. According to micro/nano-indentation tests [13–15], the white etching microstructure is 10–20% harder than the parent matrix. Transmission electron microscope (TEM) characterisation showed that WEAs consist of nano-sized dislocation cells ranging from 10 to 100 nm in size [8,15,16] and the diffraction patterns indicated this microstructure to be ferritic [15,17]. Severe plastic deformation (SPD) is believed to manifest as WEAs [18] rather than as adiabatic shearing [19], with the associated dislocation density reaching $10^{16} - 10^{17}$ m^{-2} [20]. Carbide dissolution was also found during WEA formation [8,15,20,21]. The increase in carbon content in solid

* Corresponding author.
E-mail address: p.rivera1@lancaster.ac.uk (P.E.J. Rivera-Díaz-del-Castillo).

https://doi.org/10.1016/j.actamat.2018.05.056

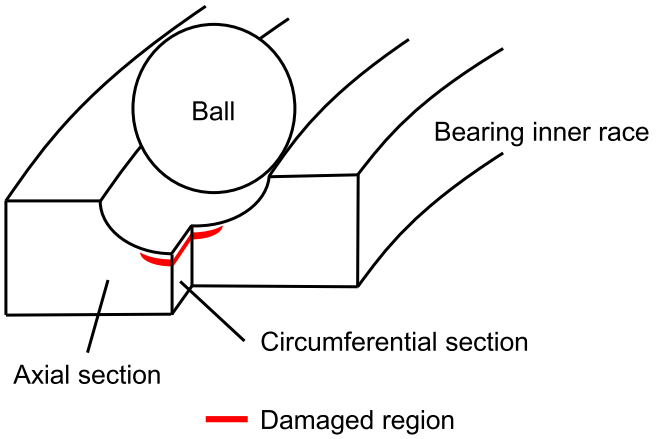

Fig. 1. Schematic of a bearing inner ring showing its axial and circumferential sections.

solution is believed to be the main reason for the distinct hardening of the resultant microstructure [15,20]. Furthermore, studies [16,22] using atom probe tomography (APT) show significant carbon segregation to dislocation cell walls with carbon depleted cell interiors. The origin of WEAs has been discussed for decades, and it is now widely accepted that WEAs stem from the repetitive rubbing of crack surfaces caused by cyclic rolling contact [7,12,23,24], and that carbon redistribution dominates their formation [16,22]. Nonetheless, a plausible physical model to describe the formation of the white etching microstructure is still unavailable, impeding the prediction of WEAs occurrence.

DERs exhibit a form of martensite decay starting to appear after $0.1L_{10}$ bearing life [25]. A DER consists of dark etching patches on the parent matrix [26]. The development of a DER with respect to the number of cycles is manifested as the increase in the area fraction of the dark patches [27,28]. Fig. 2 (b) illustrates a DER in the axial section of a fatigued bearing inner ring. The formation of DERs is believed to be strain-induced [28,29] and the responsible stress component is believed to be the orthogonal shear stress [28,30]. TEM characterisation indicated the DER microstructure to be ferrite [26], and recent APT results revealed that the excess carbon in solid solution is incorporated to pre-existing carbide precipitates during such martensite-ferrite transition [28]. The growing precipitates can also explain why the resultant microstructure exhibits a dark contrast after nital etching, given that nital attacks carbide-ferrite interfaces [31]. According to our previous work [28], carbon migration under RCF is driven by gliding dislocations, leading to the carbon redistribution in DERs.

WEBs start to occur at the late stage of bearing life, usually after $0.1L_{50}$ [25], where L_{50} is the number of stress cycles for 50% sample failure. Unlike WEAs which are always accompanied by cracks, WEBs are formed directly in DERs or in tempered martensite when the matrix hardness is below 700 HV. As shown in Fig. 2 (c), WEBs are typically inclined 30° to the over-rolling direction in the circumferential section of a fatigued bearing inner ring, and this orientation is believed to be related to the derivative stress components [32]. Electron microscopy shows that WEBs are carbon depleted ferrite bands with lenticular carbides (LCs) lying along the boundaries [33]. Such microstructure results from a carbon redistribution process where carbon in ferrite bands migrates towards the boundaries [33,34], leading to LCs precipitation. The formation of WEBs can be explained using the dislocation assisted carbon migration theory [33].

Although WEAs, DERs and WEBs display different microstructural features and occur at different stages in bearing life, they have a significant similarity: strain-induced carbon redistribution. Apart from the difference in number of stress cycles and local stress state, the major factor featuring in such microstructural alterations is the variation in carbon migration distance, which is proportional to the number of cycles required for their occurrence. For WEAs, carbon migration distance is the average radius of dislocation cells, typically tens of nanometres; while for DERs, carbon in solid solution needs to travel hundreds of nanometres to reach the pre-existing precipitates; while for WEBs, carbon needs to migrate across ferrite bands which are several micrometres in width. Such ascending trend in carbon migration distance agrees with the occurrence sequence of these microstructural alterations throughout bearing life. Considering that in our previous work [28,33] the formation mechanisms of DERs and WEBs were both explained using the dislocation-assisted carbon theory, the theory is also applied to the formation of dislocation cells in WEAs, leading to a novel model to predict WEAs appearance. This also means that all the three types of microstructural alterations under RCF can be described under a unified theory, and the entire sequence of strain-induced microstructural transitions leading to bearing failure can now be understood and quantified.

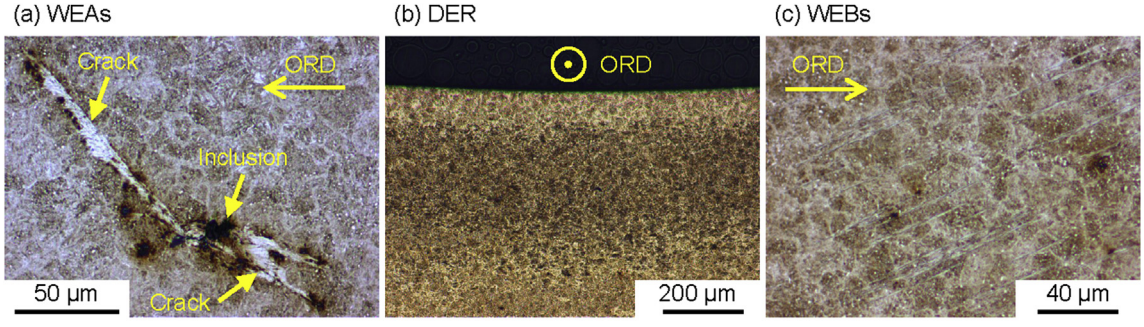

52100 bearing steel
Ball-on-rod RCF test
p_0 = 4 GPa
T = 25 °C
$\dot{N}$ = 9000 cpm
N = 5 × 10^8 cycles

52100 bearing steel
Bearing RCF test
p_0 = 3.2 GPa
T = 85 °C
$\dot{N}$ = 30000 cpm
N = 1 × 10^8 cycles

52100 bearing steel
Bearing RCF test
p_0 = 3.3 GPa
T = 70 °C
$\dot{N}$ = 30000 cpm
N = 1 × 10^9 cycles

Fig. 2. Optical images of three major types of microstructural alterations occurring under RCF and testing conditions. (a) A pair of WEAs. (b) A DER. (c) WEBs.

2. Dislocation assisted carbon migration

Under plastic deformation caused by RCF, gliding dislocations can transport carbon atoms in the solid solution owing to the unique stress history of cyclic rolling contact. This dislocation assisted carbon migration theory is schematically illustrated in Fig. 3. As shown in Fig. 3 (a), the material at the subsurface of a bearing inner ring experiences stress pulses when the balls roll over. Within each stress pulse, dislocations break out from their original Cottrell atmospheres and rapidly glide to a new position and stay immobile until the advent of next stress pulse; thus there exists a time interval (Δt) between subsequent pulses, the value of which is determined by $\dot{N}$. This time interval allows carbon in the solid solution to be captured again by mobile dislocations. The amount of carbon that can be recaptured is dependent upon Δt and the diffusivity of carbon. Hence the overall picture of this process can be described as the generation of a carbon flux as a consequence of dislocation glide. Following the previous work by the authors [33], the magnitude of such carbon flux (J_d) can be quantitatively described by:

$$J_d = \frac{\Delta\gamma\dot{N}}{b}\left[3\left(\frac{\pi}{2}\right)^{\frac{1}{3}}\left(\frac{AD}{kT\dot{N}}\right)^{\frac{2}{3}}C_V^l\right], \quad (1)$$

where $\Delta\gamma$ denotes the plastic shear strain amplitude within each stress cycle, b denotes the magnitude of Burgers vector, A denotes the interaction energy between a carbon atom and a dislocation strain field, D denotes the diffusion coefficient of carbon atoms in body-centred cubic iron, k denotes the Boltzmann constant and C_V^l denotes the background carbon concentration per unit volume. Note D is calculated via $D = D_0\exp(-E/RT)$ [35] where D_0 denotes the maximal diffusion coefficient for carbon, E denotes the activation energy for carbon diffusion and R denotes the ideal gas constant.

The presence of such dislocation-assisted carbon flux under cyclic loading leads to carbon migration that cannot be achieved by thermal activation at the bearing operation temperatures. Fig. 4 shows the calculated magnitudes of carbon flux in the martensitic matrix with respect to temperature resulting from thermal activation and dislocation glide, respectively, with the same carbon concentration background. The thermally activated carbon flux (J_t) is calculated via $J_t = -D\nabla C_V^m$. J_d is approximately 7 orders of magnitude higher than J_t at typical bearing operation temperatures, making J_t negligible compared to J_d. Therefore, the observed carbon migration in microstructural alterations under RCF such as WEAs, DERs and WEBs should be attributed to this dislocation-based theory.

3. Modelling WEA formation

3.1. Dislocation cell formation model

The microstructure within WEAs consists of nano-sized dislocation cells with carbon segregated to cell walls, which is a consequence of SPD. Under plastic deformation a large amount of dislocations can be generated, and the clustering of dislocations to

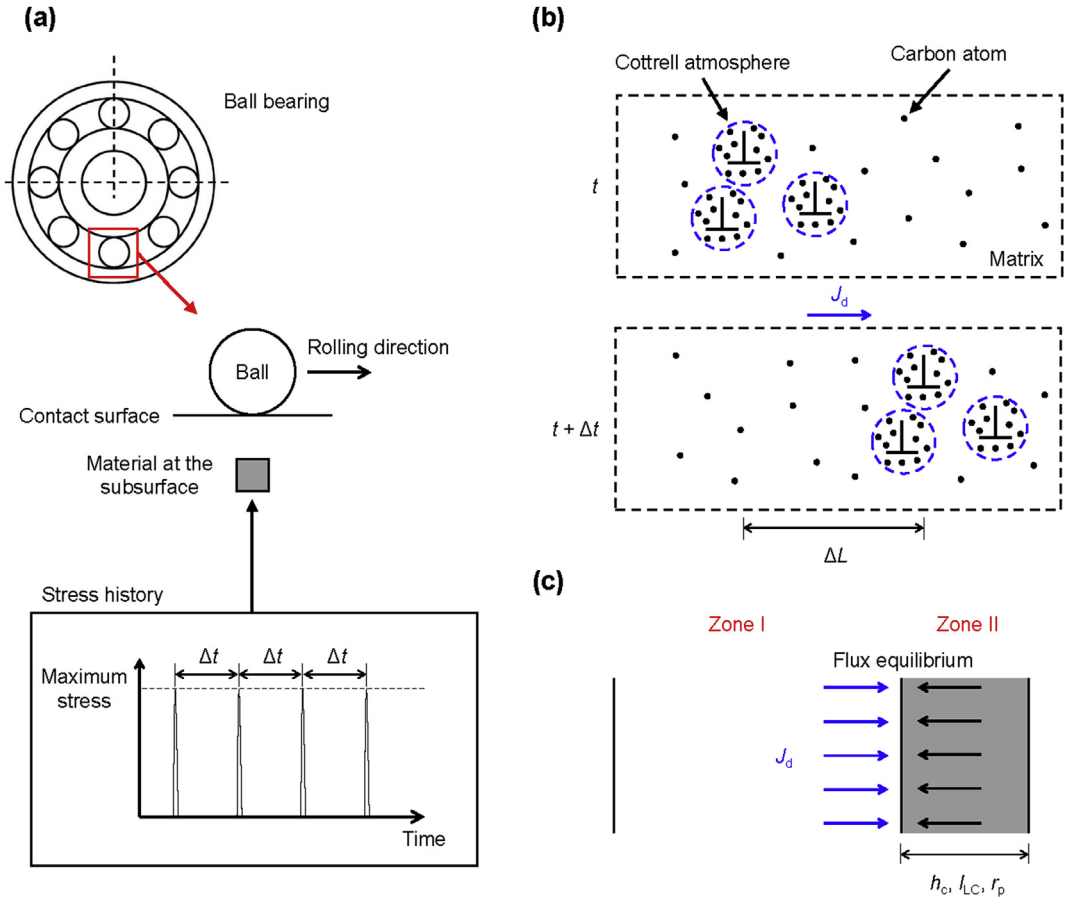

Fig. 3. Schematics showing the dislocation-assisted carbon migration theory under RCF. (a) Stress history experienced by the subsurface material in bearing inner rings. (b) Carbon atmospheres dragged by gliding dislocations. (c) Carbon segregation driven by dislocation-assisted carbon flux to different types of carbon-enriched zones.

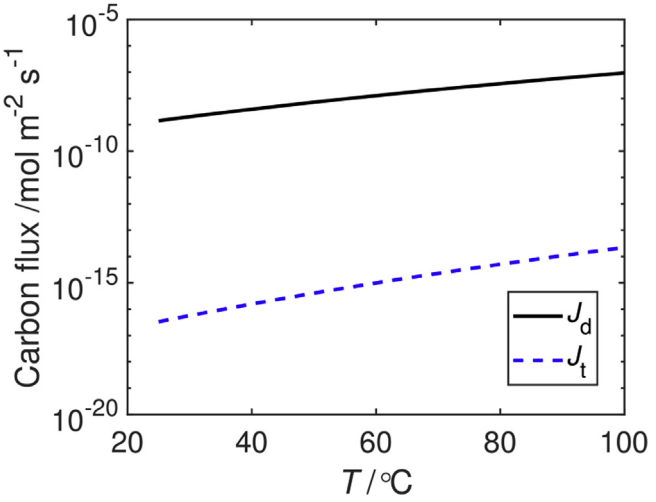

Fig. 4. Magnitudes of dislocation-assisted and thermally activated carbon flux with respect to temperature.

form cell walls becomes thermodynamically favourable [36]. Hence carbon segregation to cell walls becomes possible, because gliding dislocations can drag Cottrell atmospheres [37] around them and thus transport carbon atoms towards cell walls, and the carbon flux can be quantitatively described by Equation (1). For the case of dislocation cell formation, C_V^l, the background carbon concentration per unit volume becomes C_V^i, the carbon concentration per unit volume in the cell interiors. In this context, a dislocation cell formation model is postulated and its basic assumptions are listed as follows:

- Carbon redistribution in dislocation cells is driven by dislocation-assisted carbon migration only, and other mechanisms do not operate.
- The carbon transported to the cell walls is anchored to atmospheres around immobile dislocations that configure such walls. Therefore, it is assumed that with the dislocation-assisted carbon migration operating, the carbon concentration per unit volume in cell walls, C_V^w, is a constant equal to the saturation concentration in a Cottrell atmosphere, 7 at% [38,39].
- As summarised by Bhadeshia [7], almost all types of non-metallic inclusions in bearing steels have weak interfaces with the matrix, and significant open cavities were observed at the Al_2O_3 inclusion/matrix interface in 100Cr6 bearing steel by Hashimoto et al. [40]. Therefore, it is assumed in this model that a crack is present from the beginning of WEA formation.

As schematically shown in Fig. 5 (c), a dislocation cell is composed by two concentric spheres, with the inner one representing the cell interior and the outer layer representing the cell wall. The radius of the cell is termed r_c, and the cell wall thickness is termed h_c. During dislocation cell formation, the cell wall gradually thickens by consuming the carbon in the cell interior. Hence the carbon flux equilibrium can be obtained at the proceeding cell wall front as follows:

$$\frac{dh_c}{dN}\left(C_V^w - C_V^i\right)\dot{N} = \frac{\Delta\gamma\dot{N}}{b}\left[3\left(\frac{\pi}{2}\right)^{\frac{1}{3}}\left(\frac{AD}{kT\dot{N}}\right)^{\frac{2}{3}}C_V^i\right]. \quad (2)$$

In addition, carbon mass conservation requires:

$$\frac{4}{3}\pi r_c^3 C_V^0 = \frac{4}{3}\pi(r_c - h_c)^3 C_V^i + \frac{4}{3}\pi\left[\left(r_c^3 - (r_c - h_c)^3\right]C_V^w, \quad (3)$$

where C_V^0 is the total carbon concentration per unit volume of the system which is equal to that of the alloy by assuming complete carbide dissolution. The solution to Equations (2) and (3) can produce a curve to describe carbon depletion in the cell interior with respect to the number of cycles. In this context, the formation progress of a dislocation cell can be quantified via:

$$\text{Cell\%} = \left(1 - \frac{C_V^i}{C_V^0}\right) \times 100. \quad (4)$$

To solve the equations, the key input parameter $\Delta\gamma$ must be obtained. However, $\Delta\gamma$ cannot be directly measured but depends on the local subsurface stress state. As the SPD in WEAs is caused by the rubbing of crack surfaces, a stress state analysis for such geometry is presented.

Fig. 5 (a) shows the coordinate system for WEA formation. According to the Hertzian elastic contact theory [4], the contact surface between the ball and the raceway is an ellipse. Here the x axis is defined as the direction of the long axis of the contact ellipse, and the y axis is defined as the direction of the short axis, which is also the rolling direction of the ball, and the z axis is defined as the depth perpendicular to the contact surface. The coordinate origin is hence the centre of the contact ellipse, where the maximum contact pressure (p_0) is achieved. An Al_2O_3 inclusion located along the z axis is considered. Given the fact that the crack surfaces originating from the Al_2O_3 inclusion are always perpendicular to the predefined yz plane with an inclination angle of approximately 45° with respect to the over rolling direction (ORD) y, the maximum shear stress is considered responsible for WEA formation. Under cyclic rolling contact, the maximum shear stress is achieved when the ball is right above the inclusion [12], where the rubbing of crack surfaces occurs. At this moment, the stress component applied normal to the crack faces, p_c, is equal to $-\sin\left(\frac{\pi}{4}\right)(\sigma_{yy} + \sigma_{zz})$, where σ_{yy} and σ_{zz} are the normal stress components. Assuming the friction coefficient between the crack surfaces to be μ, the resultant traction stress on the rubbing crack faces q_c is thus μp_c. With such contact geometry of crack surfaces, the stress components are maximised at the crack surface and diminish along the depth below the crack surface. Hence the cells that are formed first are those close to the crack surfaces, where the equivalent shear stress, τ_e, can be expressed as:

$$\tau_e = \sqrt{\left(\frac{p_c}{2}\right)^2 + q_c^2}. \quad (5)$$

Given the stress state (Fig. 5 (b), the plastic response to applied cyclic loading for this steel can be obtained. If the steel is 100Cr6, for example, by referring to the experimentally obtained $\Delta\gamma$ in Ref. [41], $\Delta\gamma = 0.0003\left(\frac{\tau_a}{\tau_a^{th}} - 1\right)^3$, where τ_a denotes the applied shear stress and τ_a^{th} denotes the threshold shear stress for the onset of plastic response. In the case of WEA formation, τ_a corresponds to τ_e while τ_a^{th} corresponds to the yield shear strength of the steel, τ_Y. Therefore, for 100Cr6 bearing steel:

$$\Delta\gamma = 0.0003\left(\frac{\tau_e}{\tau_Y} - 1\right)^3. \quad (6)$$

With the dislocation assisted carbon migration operating, it can be expected that Cell% gradually increases, approaching 100 where the cell formation is completed. Given that the dislocation cells

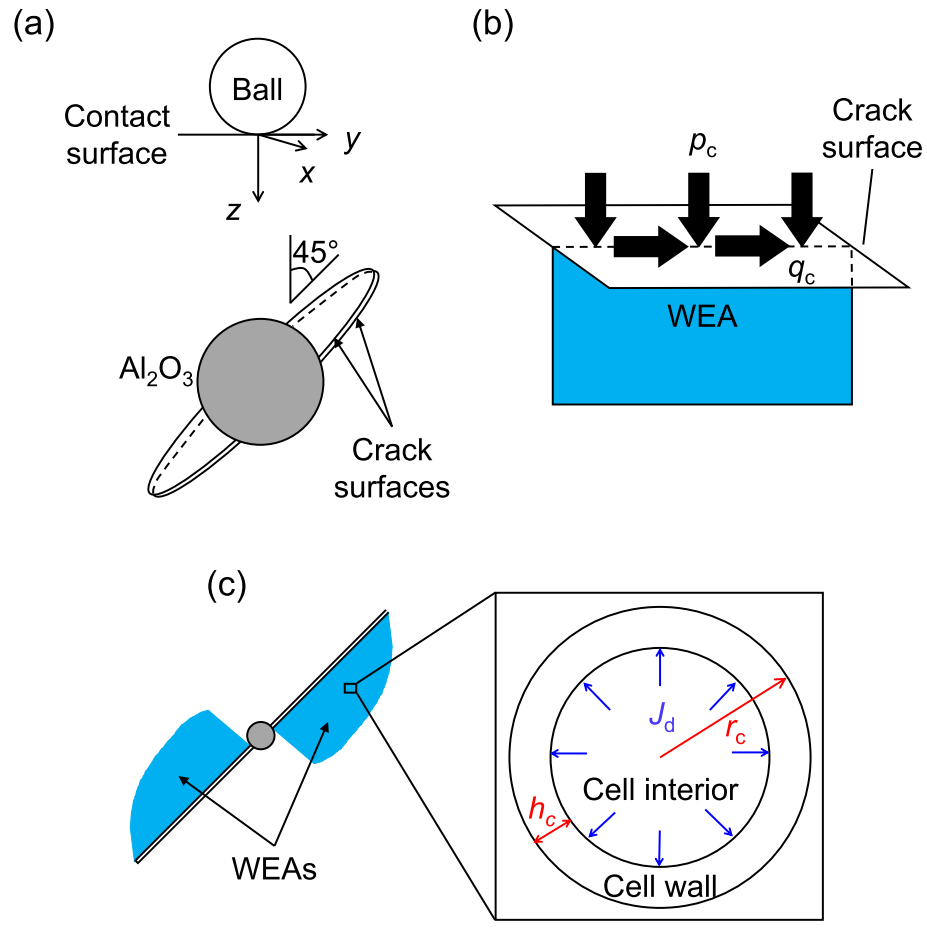

Fig. 5. (a) Defined coordinate system. (b) Stress state on rubbing crack surfaces. (c) Mechanism of dislocation cell formation in WEAs.

close to the crack surfaces are formed first, WEAs should start to appear when the formation of these cells is completed. Hence the number of cycles for the completion of cell formation close to crack surfaces is defined as the number of cycles for WEA appearance, termed N_a^{WEAs}. N_a^{WEAs} can be experimentally estimated by RCF tests.

4. Experimental validation

4.1. Ball-on-rod RCF tests and WEA detection

In order to investigate the appearance of WEAs under various contact pressures, ball-on-rod tests were carried out. The rod sample material was 100Cr6 bearing steel, quenched from 860 °C to room temperature and then tempered at 220 °C for 4 h. The resultant hardness of the steel was around 700 HV. Fig. 6 (a) shows the test rig used. According to the test principle schematically shown in Fig. 6 (b), during the rotation of the rod sample, RCF is introduced by three balls and p_0 can be varied by adjusting the load applied onto the ball cups. The balls are made of the same material as the rod samples. The tests were conducted at room temperature with a fixed rotational speed of 3600 rpm, giving a stress cycle frequency of 9000 cpm. Three p_0 values were selected for investigating the conditions leading to WEAs formation, 3.5, 4.0 and 4.5 GPa. For each stress level, tests with a predetermined number of cycles were conducted, 10^5, 10^6, 10^7, 10^8 cycles. Two prolonged tests were also conducted, 3×10^8 cycles under 3.5 GPa and 5×10^8 cycles under 4.0 GPa. Fig. 7 shows an example of a rod tested under 4.5 GPa; the optical images of the ball over-rolling tracks are also displayed. Under the same contact pressure, the ball over rolling tracks exhibit gradual darkening with increasing number of cycles, but no significant plastic deformation is found at the contact surface, indicating good lucubration during the tests.

To examine the presence of WEAs in these samples, the tracks were sectioned using the method shown in Fig. 8 (a), obtaining their circumferential sections. The polished circumferential sections were then etched with 2% nital to reveal the microstructure, especially WEAs formation. Table 1 summarises the observation results on WEAs formation. It can be seen that with increasing p_0, the number of cycles required to produce WEAs decreases. Fig. 8 (b) and (c) illustrate the first appearance of a pair of WEAs in the 3.5 GPa test after 3×10^8 cycles. A typical 45° inclination angle with respect to ORD of the WEAs is observed, and their formation depth agrees with where the maximum shear stress is. Fig. 8 (d) and (e) show the first appearance of WEAs in the 4.0 GPa test after 10^8 cycles and in the 4.5 GPa test after 10^7 cycles, respectively. At the early formation stage, these fresh WEAs are relatively small in size, whereas they can further grow under prolonged testing (Fig. 2 (a)).

4.2. Modelling results and discussion

Table 2 lists the values of the constants used for the WEAs formation model. As for μ, the most frequently used value for modelling crack propagation in such steels is 0.1–0.5 [41–43]; hence an average value of 0.3 is employed for the calculation. According to the TEM and APT observations [8,15,16], the average r_c of the cells in WEAs is 25 nm. The normal stress components, σ_{yy} and

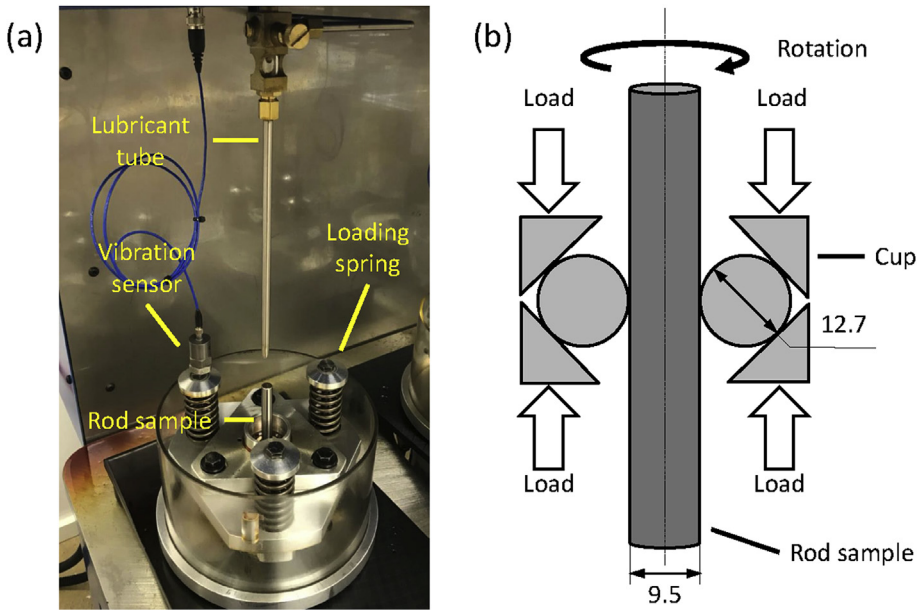

Fig. 6. (a) Three-ball-on-rod RCF tester. (b) Principle of ball-on-rod RCF tests.

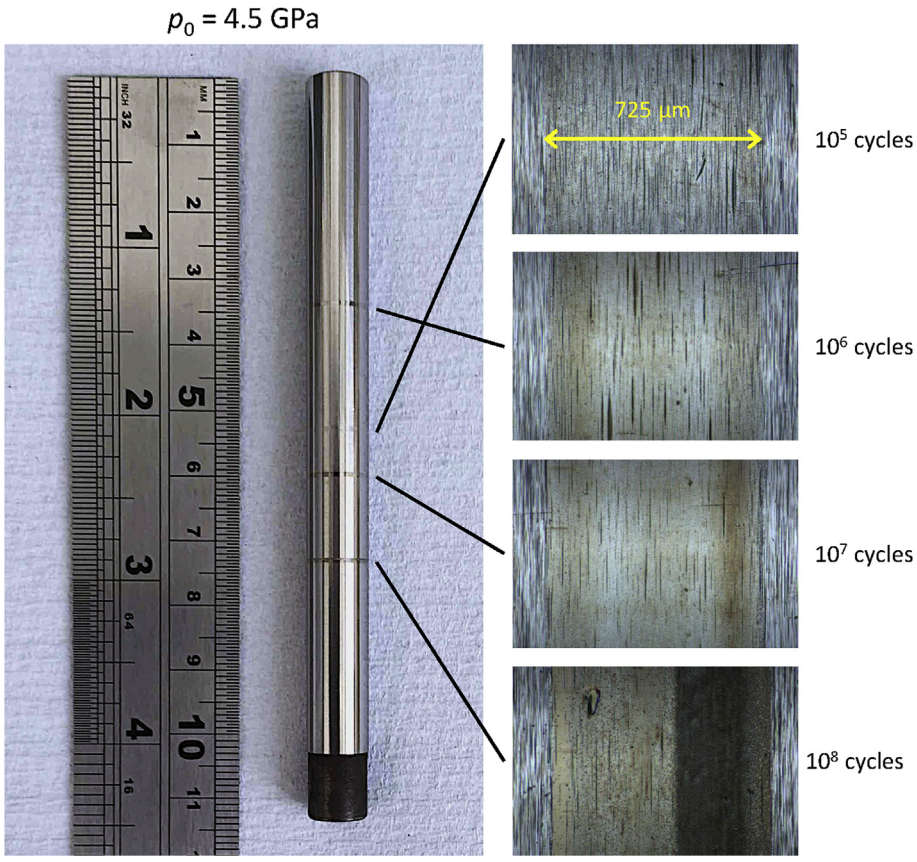

Fig. 7. Fatigued rod sample with ball over-rolling tracks.

σ_{zz}, under various contact pressures, p_0, are calculated with the Hertzian elastic contact theory [44]. The yield shear strength of the material, τ_Y, used in Equation (6) is experimentally measured by uni-axial tensile tests to be 0.74 GPa (Appendix). By inputting the testing conditions, the appearance of WEAs can be predicted. Fig. 9 (a) shows a comparison between the calculated N_a^{WEAs} curve with respect to p_0 and the experimental observation of WEA appearance in Table 1. With the given testing conditions, the model can estimate WEAs appearance with good accuracy.

Besides, the model is applied to the experimental data from the

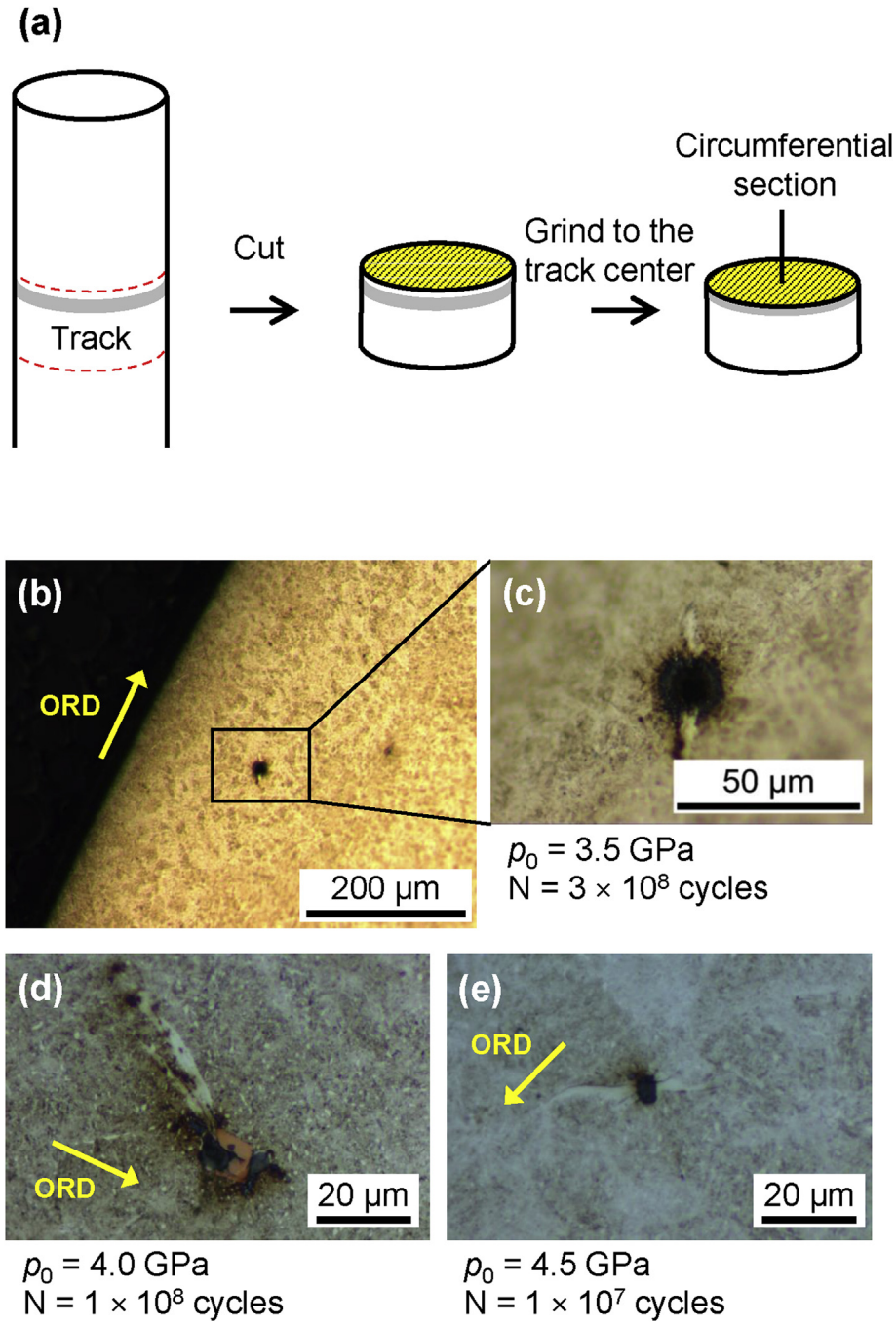

Fig. 8. Detection of WEAs in fatigued rods. (a) Method to prepare the circumferential section of a ball over-rolling track. (b)–(e) Optical images of WEAs introduced by ball-on-rod tests.

Table 1
Presence of WEAs in RCF tested samples (✓ for WEAs, ✗ for No WEAs, - for Not tested).

		p_0 (GPa)		
		3.5	4.0	4.5
N (Cycles)	10^5	✗	✗	✗
	10^6	✗	✗	✗
	10^7	✗	✗	✓
	10^8	✗	✓	-
	3×10^8	✓	-	-
	5×10^8	-	✓	-

Table 2
Values of the constants used in the dislocation cell formation model.

Constant	Value
b	0.2876 nm
A	3×10^{-30} N m^2[37]
D_0	6.2×10^{-7} m^2 s^{-1}
E	80 kJ mol^{-1}[35]
R	8.314 J K^{-1}mol^{-1}
k	1.38×10^{-23} m^2 kg s^{-2} K^{-1}

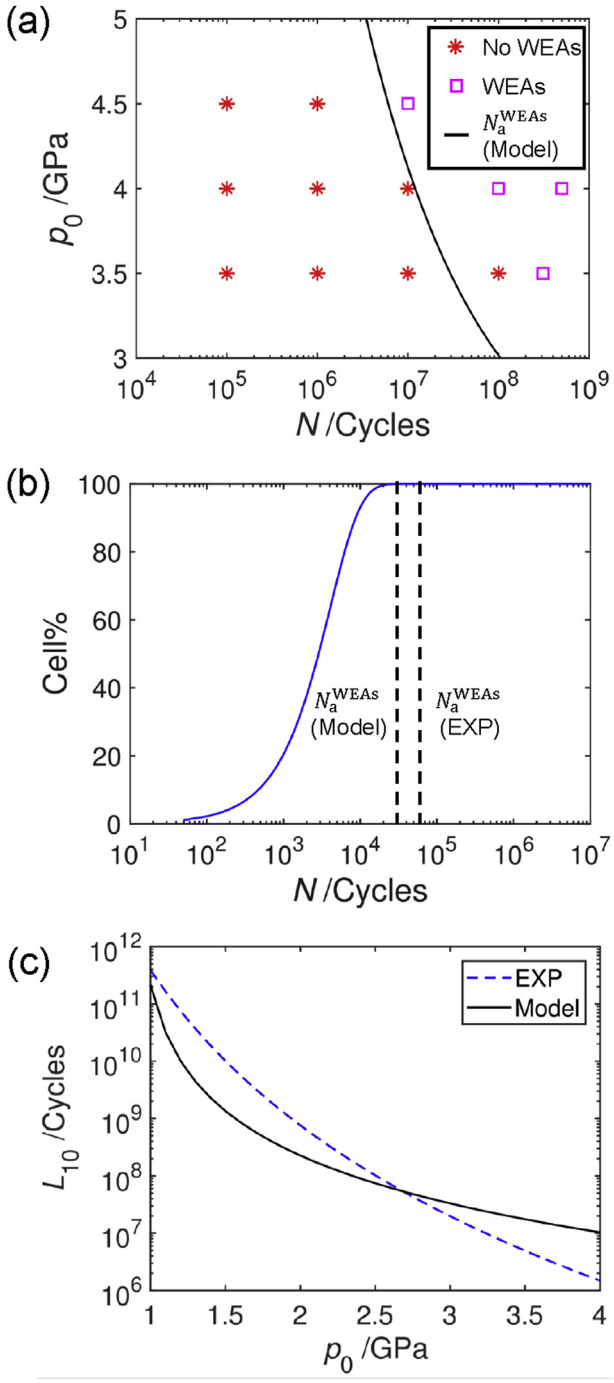

Fig. 9. Modelling results in comparison to experimental observations. (a) WEA appearance in the ball-on-rod tests. (b) WEA appearance reported by Fuurumura et al. [25] (EXP). (c) L_{10} bearing life reported by Furumura et al. [25] (EXP).

literature. Furumura et al. [25] reported the appearance of WEAs at 6×10^4 cycles in RCF tested bearing samples. The tests were conducted with a contact pressure of 3.43 GPa, a temperature of 85 °C, and a stress cycle frequency of 15000 cpm. Fig. 9 (b) shows the calculated Cell% with respect to N, and the predicted N_a^{WEAs} agrees with the experimental observation. Note that the τ_Y of the steel used in Ref. [25] was estimated to be 0.34 GPa by the uni-axial tests in Appendix.

The validation of the proposed WEAs formation model confirms the mechanism of carbon redistribution in WEAs. It is shown that the model is capable of predicting WEA appearance for various RCF testing conditions and steel types. Additionally, Furumura et al. [25] argued that N_a^{WEAs} is approximately one thousandth of L_{10} of a bearing steel, and that bearing life thus can be estimated by WEAs appearance. Following this relationship, the evolution of L_{10} with respect to p_0 predicted for the bearing steel in Ref. [25] by the WEAs formation model is shown in Fig. 9 (c), and compared to the experimental results by Furumura et al. [25] (EXP); good agreement is obtained. The estimation of bearing life is of key importance to bearing industry. Moreover, the successful application of the dislocation-assisted carbon migration mechanism leads to the establishment of a unified theory for all the three types of microstructural alterations under RCF.

5. Unified theory

5.1. Microstructural alteration models

The suggested dislocation assisted carbon migration mechanism is applied to the three types of microstructural alterations occurring at different stages of RCF. All these alterations stem from strain-induced carbon redistribution, namely carbon segregation to carbon-enriched zones.

Fig. 10 illustrates the observed carbon redistributions in WEAs, DERs and WEBs and the proposed formation models for these cases.

- For WEAs, the APT image shows evidence of carbon segregation to dislocation cell walls; the model describes the growth of carbon-enriched cell wall (with thickness h_c), leaving a carbon-depleted cell interior.
- For DERs, the APT image indicates the pre-existing precipitates to be carbon absorbers; the model describes the thickening of carbon-enriched precipitates (with half width r_p) by consuming carbon in the matrix [28].
- For WEBs, the SEM image shows obvious LC formation along the ferrite band; the model describes the growth of carbon-enriched LC (with thickness l_{LC}) by consuming carbon in the ferrite band [33].

In these models, carbon migration is assisted by gliding dislocations. As shown in Fig. 3 (c), Zone I represents the carbon-depleted zones while Zone II represents the carbon-enriched zones. The carbon flux equilibria in WEAs, DERs and WEBs can thus be generalised by the following equation:

$$\frac{\mathrm{d}(h_c, 2r_p, l_{LC})}{\mathrm{d}N}\left(C_V^{II} - C_V^{I}\right)\dot{N} = J_d, \tag{7}$$

where C_V^I and C_V^{II} denote the carbon concentrations per unit volume in Zone I and Zone II, respectively. Additionally, a carbon mass conservation equation can be obtained as follows:

$$V^0 C_V^0 = V^{II} C_V^{II} + \left(V^0 - V^{II}\right) C_V^{I}, \tag{8}$$

where V^0 and V^{II} denote the volumes of the entire system and Zone II, respectively. Equations (7) and (8) are the key equations to solving the microstructural alterations under RCF with a unified theory.

5.2. Modelling results and discussion

The proposed microstructural alteration models can quantitatively predict their formation progress. In the dislocation cell

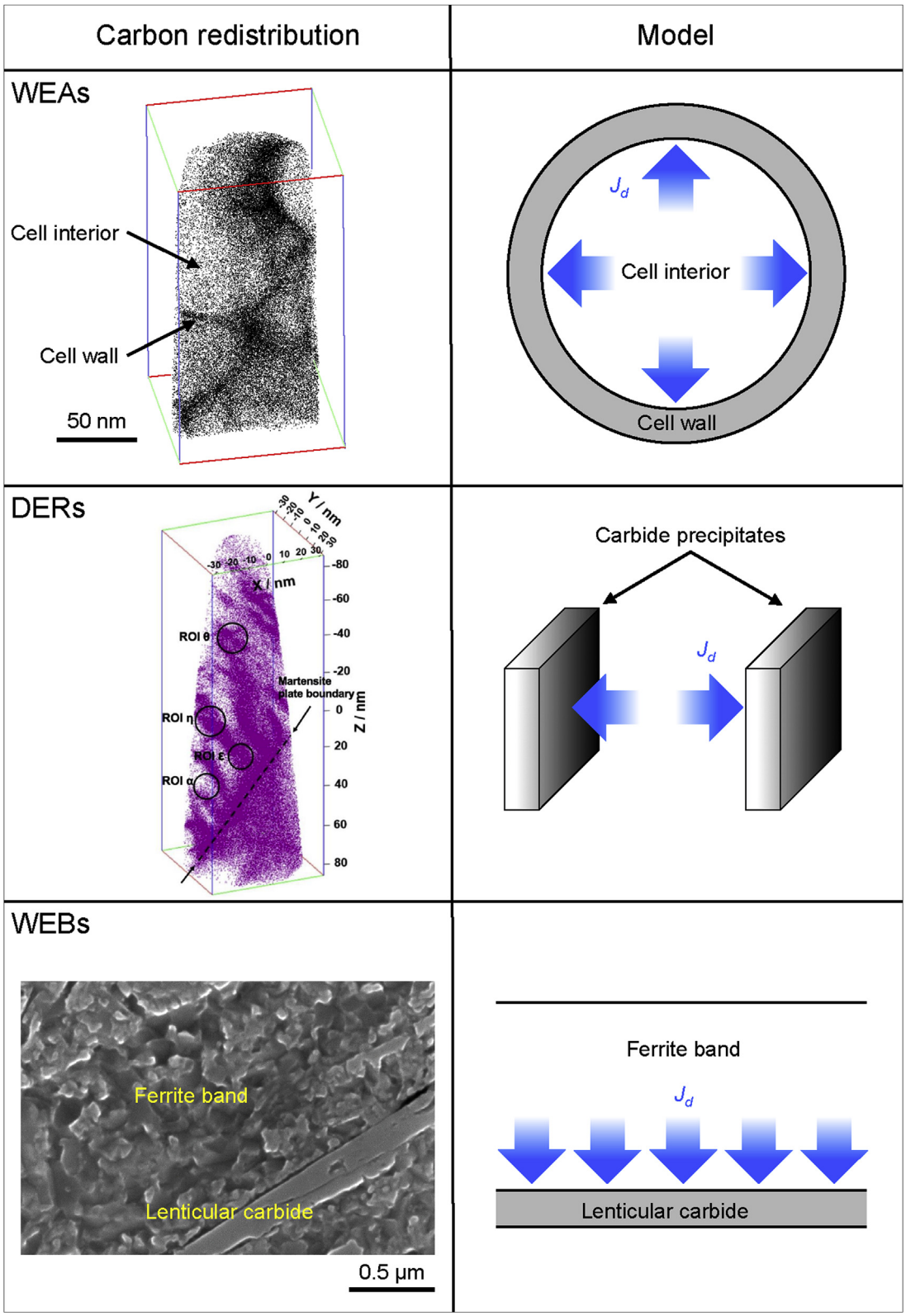

Fig. 10. Summary of the experimental evidence of carbon redistribution in WEAs, DERs and WEBs and corresponding models based on the dislocation-assisted carbon migration theory.

formation model, Cell% is defined as the extent of carbon depletion in cell interiors; in the DER model, DER% is defined as the extent of carbon depletion in the matrix; and in the WEB model, WEB% is defined as the extent of carbon depletion in ferrite bands. Fig. 11 presents the formation curves calculated by the three models using the RCF testing conditions reported by Furumura et al. [25]. According to the curves, the occurrence sequence of WEAs, DERs and WEBs through the whole bearing life is obtained. It can be seen that the major formation stage for dislocation cells is from 10^2 to 10^4 cycles, and for DERs, it is from 10^6 to 10^8 cycles, and for WEBs, it is from 10^8 to 10^{10} cycles. The most important point these curves have in common is that regardless of microstructural alteration type, the start of formation is always about 1% of the end of formation. Altering RCF testing conditions shifts the curves but does not affect such proportion. Since WEAs consist of nano-sized dislocation cells, the white etching microstructure cannot be observed before the completion of cells. Hence N_a^{WEAs} is defined as the end of dislocation cell formation curve. However, the features in DERs and WEBs (dark etching patches and LCs) are at the microscale, which makes the whole carbon redistribution progress easily captured by optical microscope. Therefore, the predicted numbers of cycles where DERs and WEBs appear, termed N_a^{DERs} and N_a^{WEBs}, should be the starting points of their formation curves, which are estimated to be 1% of the end points. In Fig. 11, the predicted N_a^{WEAs}, N_a^{DERs} and N_a^{WEBs} are compared with experimental observations, obtaining good agreement.

In this research, the three types of microstructural alterations are modelled independently using a unified approach. WEAs and WEBs do not tend to influence each other as they are both strongly localised. Conversely, DERs exhibit transitions over widespread areas. The presence of DERs does not affect the appearance of WEAs; DERs do form at times at least 2 orders of magnitude higher than those for WEAs. However, further growth of WEAs may occur within DERs, where the matrix is softened. As the resultant microstructure of WEAs is much harder than the parent martensite, an enlarged hardness difference between the two phases definitely fosters crack propagation, and consequently promotes WEA growth. Nevertheless, the extent of material softening as a result of DER formation is very limited, at most 18% hardness decrease [28]. If WEBs are formed above DERs, the calculated formation curve of WEBs will slightly shift towards a smaller number of cycles.

The effects of RCF testing conditions such as T, $\dot{N}$ and p_0 are studied in Fig. 12. In each plot, the appearance curves calculated from the models divide the space into regions with different combinations of microstructural alterations. Generally speaking, increasing T and/or p_0 can promote the formation of the microstructural alterations while increasing $\dot{N}$ decelerates their formation, although the effect of T and p_0 is significantly more pronounced than that of $\dot{N}$. These effects can be explained by referring to Equation (1). According to the dislocation assisted carbon migration theory, increasing T enhances carbon diffusivity, and consequently increases the amount of carbon that can be captured by gliding dislocations; increasing p_0 promotes dislocation glide, leading to higher J_d via higher $\Delta\gamma$; increasing $\dot{N}$, however, decreases Δt which reduces the amount of carbon that can be captured by dislocations within a stress cycle. Note that the predicted appearance curves of the microstructural alterations under varying p_0 are well validated by the experimental results by Takemura et al. [45]. This means that for any given RCF testing conditions, the RCF situation can be directly indexed from these microstructural alteration maps. Additionally, the proposed models are in agreement with the experimental results reported over the last 50 years; Table 3 summarises the microstructural alterations produced by RCF tests in the literature that can be replicated by the proposed unified theory.

6. Conclusions

The phenomenology of WEAs, DERs and WEBs formed under RCF in bearing steels has been reviewed. The governing mechanism displayed by such microstructural alterations is the strain-induced carbon redistribution. This leads to the establishment of a unified theory to explain their formation. Following the successful application of the dislocation-assisted carbon migration theory to DERs and WEBs in our previous work, the theory is now applied to WEAs. A dislocation cell formation model has been proposed to describe carbon segregation to cell walls during WEA formation. The model yields predictions of WEAs appearance. Three-ball-on-rod tests were carried out to investigate WEAs appearance under various contact pressures, with the experimental observations being in agreement with the modelling results. The WEAs appearance model is also validated by data reported in the literature. Also, the model is capable of estimating bearing life with good accuracy. Finally, the three microstructural alteration models are combined

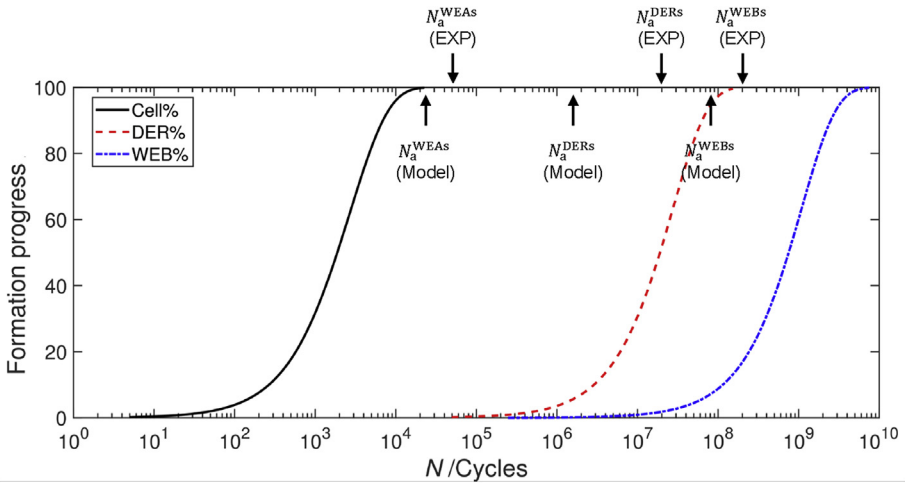

Fig. 11. Calculated formation curves for WEAs, DERs and WEBs. The predictions three types of microstructural alterations occurrence are compared with the experimental observations by Furumura et al. [25] (EXP). The test was conducted at p_0 = 3.43 GPa.

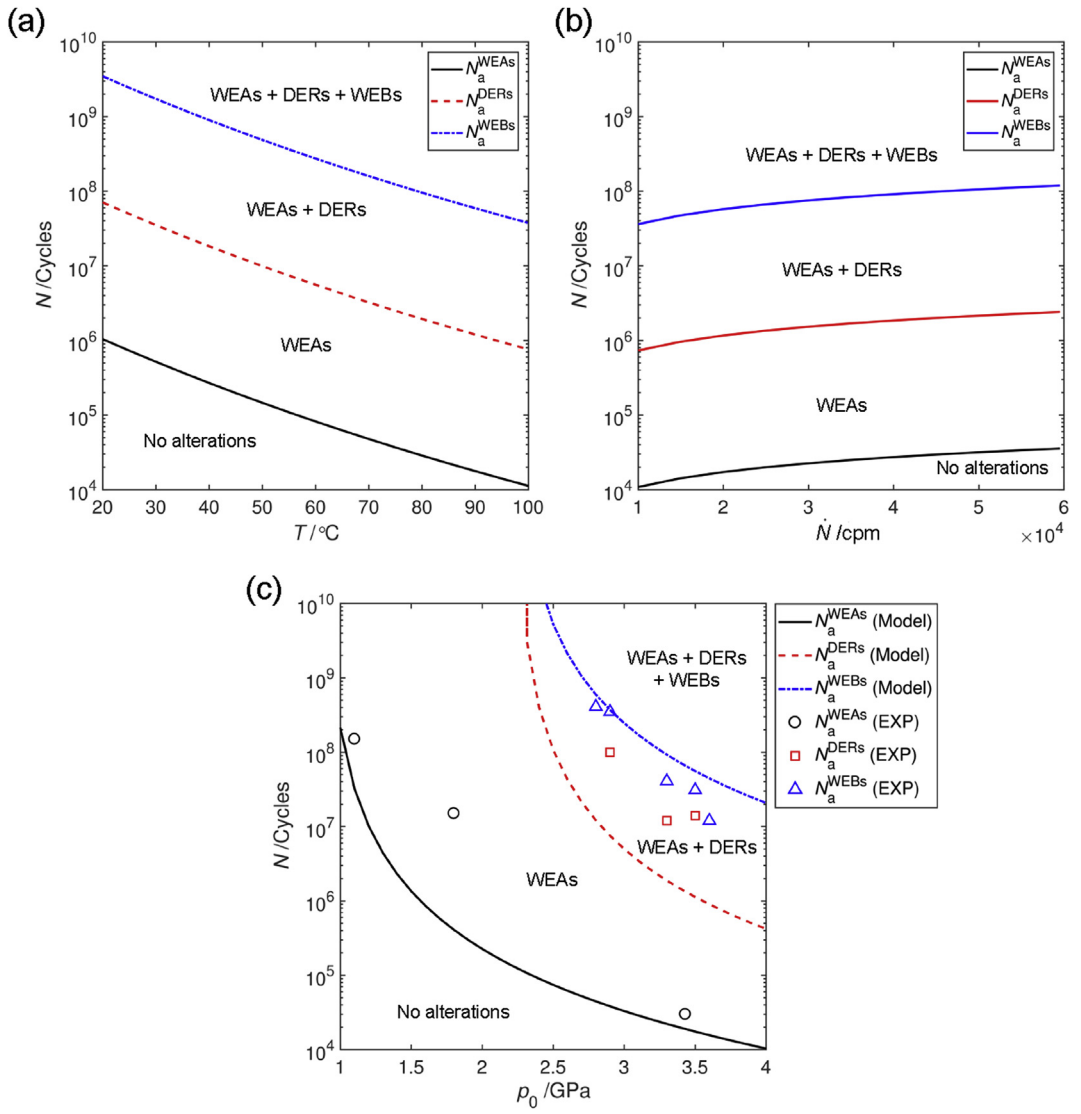

Fig. 12. Microstructural alterations maps for varying T (a), $\dot{N}$ (b) and p_0 (c). The experimental results in (c) are reported by Takemura et al. [45] (EXP). For the calculations in (a), $p_0 = 3.4$ GPa, $\dot{N} = 3 \times 10^4$ cpm. For the calculations in (b), $p_0 = 3.4$ GPa, $T = 85\,^{\circ}$C. For the calculations in (c), $\dot{N} = 3 \times 10^4$ cpm, $T = 85\,^{\circ}$C.

Table 3
Summary of microstructural alterations produced by RCF tests in the literature replicated by the proposed model.

Reference	Testing method	p_0 /GPa	T/°C	$\dot{N}$/cpm	Modelled alterations
[27]	Full-scale bearing	3.24 & 3.58	30	1×10^4	DERs
[46]	Full-scale bearing	3.27	95–100	4.8×10^4	WEBs
[34]	Full-scale bearing	3.4	95–100	4.8×10^4	WEBs
[30]	Full-scale bearing	3.3	60	3×10^4	DERs
[26]	Full-scale bearing	3.28 & 3.72	50–55	3×10^4	DERs & WEBs
[47]	Full-scale bearing	3.28 & 3.72	53	3×10^4	DERs & WEBs
[6]	Ball-on-rod	5.9	85	4.6×10^4	DERs & WEBs
[48]	Radial-type	4.9	60	9.4×10^2	DERs
[25]	Full-scale bearing	3.43	50–130	3×10^4	WEAs
[45]	Full-scale bearing	1.20–3.43	50–130	3×10^4	WEAs & DERs & WEBs
[49]	Ball-on-rod	5.9	25	4.6×10^4	DERs
[49]	Ball-on-pivot	5.3	150	3.4×10^4	WEBs
[33]	Full-scale bearing	3.30	70	3×10^4	WEBs
[28]	Full-scale bearing	3.24	83	3×10^4	DERs

and, for the first time, it becomes possible to predict the occurrence and the formation progress of WEAs, DERs and WEBs with a unified theory. A new concept of microstructural maps is introduced; such maps describe WEA/DER/WEB transitions as a function of temperature, contact pressure, stress cycle frequency and number of cycles. The new theory correctly predicts the results reported in the literature in the last 50 years.

Acknowledgements

This work was financed by grant EP/L014742/1 from the UK Engineering and Physical Sciences Research Council (EPSRC). PEJRDC is grateful to the Royal Academy of Engineering Grant number (RCSRF1718\5\32) for funding a Research Chair.

Appendix

Tensile tests were carried out on a Mayes 100 KN LCF mechanical tester to measure the yield shear strength (τ_Y) of 100Cr6 bearing steels with two standard heat treatments. S1 represents the steel quenched and then tempered at 220 °C for 4 h, corresponding to the sample material for the three ball-on-rod tests in this research; S2 represents the steel quenched and then tempered at 160 °C for 1.5 h, corresponding to the sample material for the bearing tests in Refs. [25] and [45]. Fig. A1 (a) shows the tensile specimen used and Fig. A1 (b) schematically shows the principle of the tensile tests. For each type of heat treatment, 5–7 tests were conducted and the representative stress-strain curves are presented in Fig. A2.

The yield tensile strength (σ_Y) can be determined from the stress-strain curves. For S1, $\sigma_Y = 1.28$ GPa; and for S2, $\sigma_Y = 0.59$ GPa. According to the von Mises criterion, $\tau_Y = \frac{\sigma_Y}{\sqrt{3}}$, hence for S1, $\tau_Y = 0.74$ GPa; and for S2, $\tau_Y = 0.34$ GPa.

References

[1] P.E.J. Rivera-Díaz-del Castillo, Rolling Contact Fatigue In Bearings: Phenomenology And Modelling Techniques, In: Bearing Steel Technologies: 9th Volume, Advances In Rolling Contact Fatigue Strength Testing And Related Substitute Technologies, ASTM International STP1548, 2012.
[2] A. Warhadpande, F. Sadeghi, R.D. Evans, Microstructural alterations in bearing steels under rolling contact fatigue Part 1 – historical overview, Tribol. Trans. 56 (3) (2013) 349–358.
[3] F. Sadeghi, B. Jalalahmadi, T. S. Slack, N. Raje, N. K. Arakere, A review of rolling contact fatigue, J. Tribol. 131(4).
[4] K. Johnson, Contact Mechanics, Cambridge University Press, 1987.
[5] J.-H. Kang, B. Hosseinkhani, P.E.J. Rivera-Díaz-del Castillo, Rolling contact fatigue in bearings: multiscale overview, Mater. Sci. Technol. 28 (1) (2012) 44–49.
[6] T. Ochi, Y. Kusano, Change in microstructure and properties in the rolling contact fatigue of bearing steel, Nippon Steel Tech. Rep. (80).
[7] H.K.D.H. Bhadeshia, Steels for bearings, Prog. Mater. Sci. 57 (2) (2012) 268–435.
[8] A. Grabulov, U. Ziese, H.W. Zandbergen, TEM/SEM investigation of microstructural changes within the white etching area under rolling contact fatigue and 3-D crack reconstruction by focused ion beam, Scripta Mater. 57 (7) (2007) 635–638.
[9] B. Loy, R. McCallum, Mode of formation of spherical particles in rolling contact fatigue, Wear 24 (2) (1973) 219–228.
[10] J.F. Braza, P.K. Pearson, C.J. Hannigan, The performance of 52100, M-50, and M-50 Nil steels in radial bearings, SAE Trans. 102 (1993) 437.
[11] G. Guetard, I. Toda-Caraballo, P.E.J. Rivera-Díaz-del Castillo, Damage evolution around primary carbides under rolling contact fatigue in VIM–VAR M50, Int. J. Fatig. 91 (2016) 59–67.
[12] M.H. Evans, Mater. Sci. Technol. 28 (1) (2012) 3–22.
[13] W. Solano-Alvarez, H.K.D.H. Bhadeshia, White-etching matter in bearing steel.

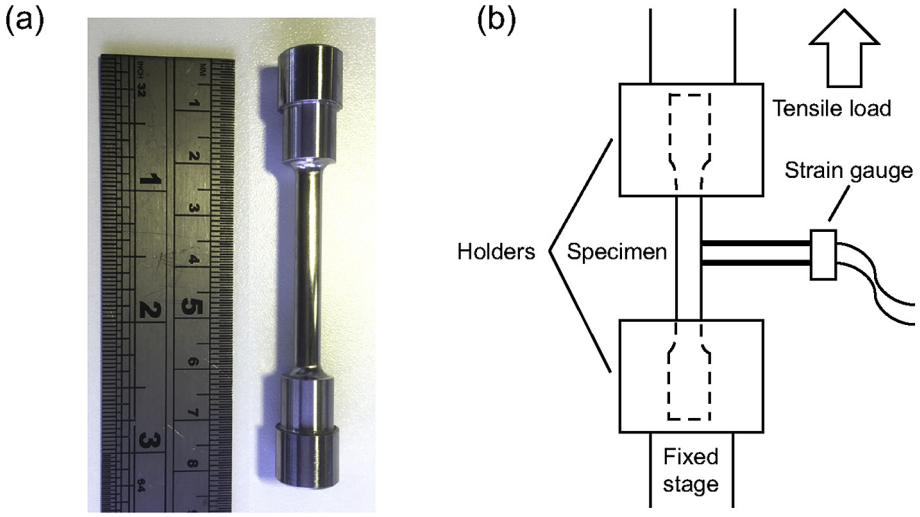

Figure A1. (a) Tensile specimen. (b) Principle of the tensile tests.

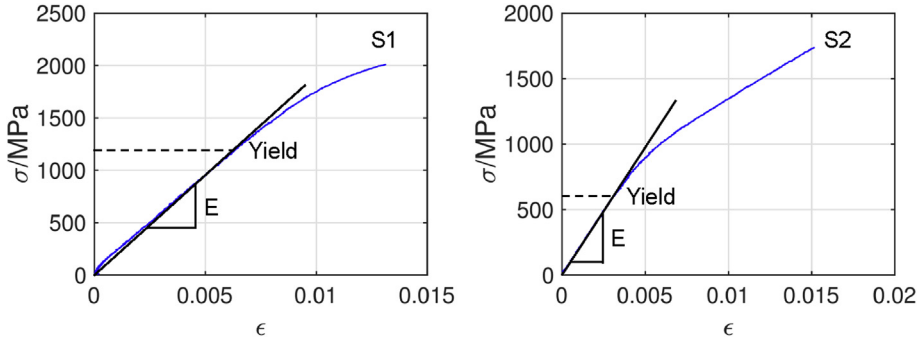

Figure A2. Stress-strain curves of S1 and S2.

Part I: controlled cracking of 52100 steel, Metall. Mater. Trans. 45 (11) (2014) 4907–4915.
[14] W. Solano-Alvarez, H.K.D.H. Bhadeshia, White-etching matter in bearing steel. Part II: distinguishing cause and effect in bearing steel failure, Metall. Mater. Trans. 45 (11) (2014) 4916–4931.
[15] P.C. Becker, Microstructural changes around non-metallic inclusions caused by rolling-contact fatigue of ball-bearing steels, Met. Technol. 8 (1) (1981) 234–243.
[16] J.H. Kang, B. Hosseinkhani, C.A. Williams, M.P. Moody, P.A.J. Bagot, P.E.J. Rivera-Díaz-del Castillo, Solute redistribution in the nanocrystalline structure formed in bearing steels, Scripta Mater. 69 (8) (2013) 630–633.
[17] M.H. Evans, J.C. Walker, C. Ma, L. Wang, R.J.K. Wood, A FIB/TEM study of butterfly crack formation and white etching area (WEA) microstructural changes under rolling contact fatigue in 100Cr6 bearing steel, Mater. Sci. Eng. A 570 (2013) 127–134.
[18] K. Hiraoka, White-type microstructural change in rolling contact fatigue from the viewpoint of severe plastic deformation, Tetsu-To-Hagane J. Iron Steel Inst. Jpn. 94 (12) (2008) 636–643.
[19] W. Solano-Alvarez, J. Duff, M.C. Smith, H.K.D.H. Bhadeshia, Mater. Sci. Technol. 33 (3) (2017) 307–310.
[20] A. Grabulov, R. Petrov, H.W. Zandbergen, EBSD investigation of the crack initiation and TEM/FIB analyses of the microstructural changes around the cracks formed under rolling contact fatigue (RCF), Int. J. Fatig. 32 (3) (2010) 576–583.
[21] J.L. O'Brien, A.H. King, Electron microscopy of stress-induced structural alterations near inclusions in bearing steels, J. Basic Sci. Eng. 88 (3) (1966) 568–571.
[22] Y.J. Li, M. Herbig, S. Goto, D. Raabe, Atomic scale characterization of white etching area and its adjacent matrix in a martensitic 100Cr6 bearing steel, Mater. Char. 123 (2017) 349–353.
[23] R.H. Vegter, J.T. Slycke, The role of hydrogen on rolling contact fatigue response of rolling element bearings, J. ASTM Int. (JAI) 7 (2) (2009) 1–12.
[24] H.K.D.H. Bhadeshia, W. Solano-Alvarez, Critical assessment 13: elimination of white etching matter in bearing steels, Mater. Sci. Technol. 31 (9) (2015) 1011–1015.
[25] K. Furumura, Y. Murakami, T. Abe, Development of long life bearing steel for full film lubrication and for poor and contaminated lubrication, Motion Contr. 1 (1996) 30–36.
[26] H. Swahn, P.C. Becker, O. Vingsbo, Martensite decay during rolling contact fatigue in ball bearings, Metallurgical transactions A 7 (8) (1976) 1099–1110.
[27] J.J. Bush, W.L. Grube, G.H. Robinson, Microstructural and residual stress changes in hardened steel due to rolling contact, Transactions of the ASM 54 (1961) 390–412.
[28] H. Fu, W. Song, E.I. Galindo-Nava, P.E.J. Rivera-Díaz-del Castillo, Strain-induced martensite decay in bearing steels under rolling contact fatigue: modelling and atomic-scale characterisation, Acta Mater. 139 (2017) 163–173.
[29] J.H. Kang, B. Hosseinkhani, R.H. Vegter, P.E.J. Rivera-Díaz-del Castillo, Modelling dislocation assisted tempering during rolling contact fatigue in bearing steels, Int. J. Fatig. 75 (2015) 115–125.
[30] T. Lund, Structural alterations in fatigue-tested ball-bearing steel, Jemkonter, Ann. For. 153 (1969) 337–343.
[31] F.S. William, J. Hashemi, Foundations of Materials Science and Engineering, McGraw-Hill, 2011.
[32] I.A. Polonsky, L.M. Keer, On white etching band formation in rolling bearings, J. Mech. Phys. Solid. 43 (4) (1995) 637–669.
[33] H. Fu, E.I. Galindo-Nava, P.E.J. Rivera-Díaz-del Castillo, Modelling and characterisation of stress-induced carbide precipitation in bearing steels under rolling contact fatigue, Acta Mater. 128 (2017) 176–187.
[34] J. Buchwald, R.W. Heckel, An analysis of microstructural changes in 52100 steel bearings during cyclic stressing (microstructural changes in 52100 steel bearing inner rings during cyclic stressing, obtaining thickening rate data on white-etching regions and lenticular carbides), ASM Transactions Quarterly 61 (1968) 750–756.
[35] H.K.D.H. Bhadeshia, R. Honeycombe, Steels: Microstructure and Properties, Butterworth-Heinemann, 2011.
[36] E.I. Galindo-Nava, P.E.J. Rivera-Díaz-del Castillo, A thermodynamic theory for dislocation cell formation and misorientation in metals, Acta Mater. 60 (11) (2012) 4370–4378.
[37] A.H. Cottrell, B.A. Bilby, Dislocation theory of yielding and strain ageing of iron, Proc. Phys. Soc. 62 (1) (1949) 49.
[38] J. Wilde, A. Cerezo, G.D.W. Smith, Three-dimensional atomic-scale mapping of a Cottrell atmosphere around a dislocation in iron, Scripta Mater. 43 (1) (2000) 39–48.
[39] D.H. Sherman, S.M. Cross, S. Kim, F. Grandjean, G.J. Long, M.K. Miller, Characterization of the carbon and retained austenite distributions in martensitic medium carbon, high silicon steel, Metall. Mater. Trans. 38 (8) (2007) 1698–1711.
[40] K. Hashimoto, T. Fujimatsu, N. Tsunekage, K. Hiraoka, K. Kida, E.C. Santos, Effect of inclusion/matrix interface cavities on internal-fracture-type rolling contact fatigue life, Mater. Des. 32 (10) (2011) 4980–4985.
[41] G.T. Hahn, V. Bhargava, C.A. Rubin, Q. Chen, K. Kim, Analysis of the rolling contact residual stresses and cyclic plastic deformation of sae 52100 steel ball bearings, J. Tribol. 109 (4) (1987) 618–626.
[42] A.D. Hearle, K.L. Johnson, Mode ii stress intensity factors for a crack parallel to the surface of an elastic half-space subjected to a moving point load, J. Mech. Phys. Solid. 33 (1) (1985) 61–81.
[43] D. Canadinc, H. Sehitoglu, K. Verzal, Analysis of surface crack growth under rolling contact fatigue, Int. J. Fatig. 30 (9) (2008) 1678–1689.
[44] A. Sackfield, D.A. Hills, D. Nowell, Mechanics of Elastic Contacts, Elsevier, 2013.
[45] H. Takemura, Y. Matsumoto, Y. Murakami, Development of a new life equation for ball and roller bearings, Tech. rep. (2000). SAE technical paper 2000-01-2601.
[46] J.A. Martin, S.F. Borgese, A.D. Eberhardt, Microstructural alterations of rolling – bearing steel undergoing cyclic stressing, J. Fluid Eng. 88 (3) (1966) 555–565.
[47] A.P. Voskamp, R. Österlund, P.C. Becker, O. Vingsbo, Gradual changes in residual stress and microstructure during contact fatigue in ball bearings, Met. Technol. 7 (1) (1980) 14–21.
[48] K. Sugino, K. Miyamoto, M. Nagumo, K. Aoki, Structural alterations of bearing steels under rolling contact fatigue, Trans. Iron Steel Inst. Jpn. 10 (2) (1970) 98.
[49] H. Muro, N. Tsushima, Microstructural, microhardness and residual stress changes due to rolling contact, Wear 15 (5) (1970) 309–330.